

Influence of microstructure on magnetic and dielectric performance of Bi₂O₃-doped Mg–Cd ferrites for high frequency antennas

Gongwen Gan^{a,*}, Dainan Zhang^{a,**}, Qing Zhang^d, Gang Wang^a, Xin Huang^a, Yan Yang^{a,b}, Yiheng Rao^a, Jie Li^a, Fang Xu^a, Xueying Wang^a, Ray T. Chen^c, Huaiwu Zhang^a

^a State Key Laboratory of Electronic Thin Films and Integrated Devices, University of Electronic Science and Technology of China, Chengdu, 610054, China

^b College of Communication Engineering, Chengdu University of Information Technology, China

^c Microelectronic Research Center, Department of Electrical and Computer Engineering, University of Texas at Austin, Austin, TX, 78758, USA

^d Institute of Chemical Materials, China Academy of Engineering Physics, China



ARTICLE INFO

Keywords:

Mg_{0.6}Cd_{0.4}Co_{0.05}Fe_{1.95}O₄ ferrites
Bi₂O₃ doping
Enhanced magnetization
Equivalent permeability and permittivity
Low loss

ABSTRACT

The effects of microstructure on the magnetic and dielectric properties of Mg_{0.6}Cd_{0.4}Co_{0.05}Fe_{1.95}O₄ spinel ferrites with the addition of 2.5 wt% Bi₂O₃ are investigated mainly for high frequency applications. The measurement results reveal that composites processed via low temperature co-fired ceramic (LTCC) technology at different sintering temperatures (900 °C, 920 °C, 930 °C, and 940 °C) possess excellent equivalent permeability (μ') and permittivity (ϵ') (at 940 °C, $\mu' \approx \epsilon' \approx 25$), over a long frequency range from 1 to 100 MHz. The results also indicate that densification sintering results in ultra low dielectric loss $\tan\delta_\epsilon$ and magnetic loss $\tan\delta_\mu$ ($\tan\delta_\epsilon \approx 0.003$, $\tan\delta_\mu \approx 0.035$). In addition, the samples present enhanced magnetic properties, such as high saturation magnetization (approximately 37.94 emu/g) and appropriate coercivity (approximately 60.5 Oe) at 940 °C. This research presents the prospect of wide application of Mg–Cd ferrites in high frequency applications.

1. Introduction

Antennas, as irreplaceable transmitter-receiver devices in wireless communication systems, have been bestowed with considerable requirements, such as miniaturization, low loss, light weight, and greater ease of integration. On these premise of the performance requirements, it is a challenge to realize a reduction in the size of traditional high frequency antennas with frequency bands from HF to VHF (2–300 MHz) [1–4]. The problem can be solved with new options provided by the timely appearance of materials processed by LTCC technology, which simultaneously holds a dominant position in system-level electronic encapsulation [5]. A sintering temperature lowered to less than 950 °C allows ceramic ferrites to be co-fired with Ag to obtain integrated multilayer RF electrical products. Not only do they have a high refractive factor n ($n = (\mu'\epsilon')^{1/2}$, $n > 1$), which enables a higher transmission speed inside the materials [1], but the miniaturization of the antenna is also realized. The resonant wavelength, is derived from the following relationship [6]:

$$\lambda = \lambda_0 / (\mu_r^* \epsilon_r)^{1/2}$$

Where μ_r and ϵ_r are the non-unity relative magnetic permeability and

dielectric permittivity of the substrate material, respectively, and λ_0 is the free space wavelength. It is observed that the resonant wavelength decreases when μ_r and ϵ_r are comparably large. However, the performance of the antenna deteriorates, i.e., low gain, low radiation efficiency and narrow bandwidth, under the condition that ϵ_r is much too high. Importantly, another cause of poor antenna performance is mismatched impedance between the antenna and free space [1,7–10]. Thus, materials that possess excellent magnetic and dielectric properties are favored by many researchers, as the magnetic and dielectric performance are coincidentally demanded by modern antennas, which are tending toward miniaturization and integration, and more importantly, good impedance matching with air [11–13]. To realize the above-mentioned characteristics, equivalent permeability and permittivity should be satisfied. The impedance of the substrate is derived from the following equation [14]:

$$Z = (\mu'\mu'_0/\epsilon'\epsilon'_0)^{1/2} = \eta_0(\mu'/\epsilon')^{1/2}$$

Where $\eta_0 = (\mu'_0/\epsilon'_0)^{1/2}$, is the impedance of air space. When $\mu'/\epsilon' \approx 1$, and $Z \approx \eta_0$, a wide bandwidth and powerful radiation efficiency are obtained.

Mg ferrite with a spinel structure is an outstanding magnetic and

* Corresponding author.

** Corresponding author.

E-mail addresses: gonggwen@gmail.com (G. Gan), dnzhang@uestc.edu.cn (D. Zhang).

dielectric material, widely used in high frequency applications, for its high permeability, low loss, and chemical and physical stability [15,16]. Surveys of the structural, electric, and magnetic characterization of Cd-substituted Mg ferrite have been undertaken [17–20]. And the effect of different Bi^{3+} ion-doped ferrites has been extensively studied [11,14,21]. It is proven that Bi_2O_3 aids work well in lowering sintering temperature, as well as tailoring magnetic and dielectric properties.

In this study, a new formula, $\text{Mg}_{0.6}\text{Cd}_{0.4}\text{Co}_{0.05}\text{Fe}_{1.95}\text{O}_4$, is put forward and synthesized by the conventional solid-state reaction method with 2.5 wt% Bi_2O_3 doping. The sintering temperature was varied from 900 °C to 940 °C to determine the correct temperature to realize permeability and permittivity matching, as well as to measure the microstructure, magnetization, and low-loss characteristics.

2. Experiment

Spinel $\text{Mg}_{0.6}\text{Cd}_{0.4}\text{Co}_{0.05}\text{Fe}_{1.95}\text{O}_4$ ferrites with Bi_2O_3 dopant were synthesized by LTCC technology. The pure raw materials, including analytical-grade MgO , CdO , Co_2O_3 , and Fe_2O_3 were weighed, mixed, and ball-milled in a planetary mixer for 12 h. After drying, the powders were presintered at 1000 °C for 4 h. After adding 2.5 wt% Bi_2O_3 , the preliminary sintered powder was again ball-milled for another 12 h. The dried powder was then ground into particles with polyvinyl alcohol (PVA) as a binder. High pressure, up to 8 MPa, was applied to press the particles into circular wafers of a certain size. In the end, the molded samples were sintered at 900 °C, 920 °C, 930 °C, 940 °C for 4 h separately.

X-ray diffraction (XRD), (DX-2700, Haoyuan Co.) measurements with Cu-K α radiation at a θ -2 θ geometric angle from 20° to 120° showed the crystallography of the samples sintered at different temperatures. Afterward, the specific crystal structure was ascertained via Rietveld refinement, performed by GASA refinement software. During the refinement progress, it was assumed that the content of the Mg ions was x , the content of Cd ions was $1-x-\zeta$, and the content of Fe ions was ζ , thus the ions occupying A-site and B-site were determined as follows, based on the cation distribution formula.

$$(\text{Mg}_x\text{Cd}_{1-x-\zeta}\text{Fe}_\zeta)^{\text{A}}[\text{Mg}_{0.6-x}\text{Cd}_{x+\zeta-0.6}\text{Fe}_{1.95-\zeta}\text{Co}_{0.05}]^{\text{B}}\text{O}_4$$

The determination of the secondary composition was carried out at the same time. Results were finally obtained after a series of fittings and iterations.

A HP-42391B RF impedance analyzer was used to measure the complex permeability and complex permittivity, using a frequency range from 1 MHz to 1.5 GHz. The microtopography was captured by scanning electron microscopy (SEM), (JEOL, JSM-6490) at a 6000 \times magnification. The hysteresis loops were measured by a vibrating sample magnetometer (VSM), (MODEL, BHL-525). X-ray Photoelectron Spectroscopy (XPS), (Thermo Fisher Scientific K-Alpha, USA) was utilized with an Al K α excitation light source and a voltage of 5 kV at room temperature to validate the valence states of the constituent elements. The measured data were then fitted by deconvolution with the fitting software XPSPEAK 4.1. Thus, the valence states of Fe^{2+} and Fe^{3+} were determined.

3. Results and discussion

Fig. 1 displays the XRD patterns of the Mg–Cd–Co ferrites sintered at different temperatures (T). With the addition of 2.5 wt% Bi_2O_3 aids, all the samples crystallized in a spinel structure and revealed standard MgFe_2O_4 peaks, matching well with the diffraction reference of standard PDF card No. 22-1086. In addition, a kind of minor low intensity impurity peak was detected with reference to $\text{Bi}_{24}\text{Fe}_2\text{O}_{39}$ (BFO) standard (JCPDS file No.42-0201). This suggested that the target objects, spinel Mg ferrites with magnetic properties and BFO with dielectric

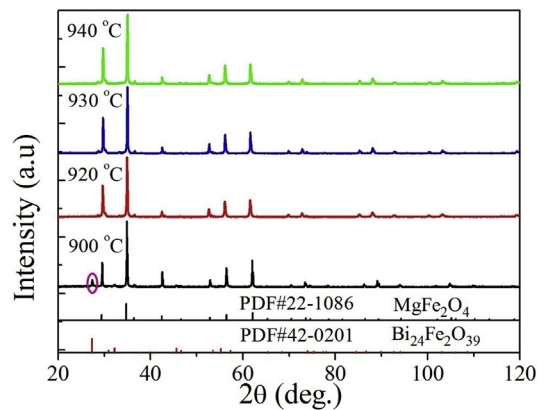


Fig. 1. XRD patterns of samples with various sintering temperature points.

properties were formed as expected, meaning that superfluous Bi^{3+} ions combined with Fe^{3+} BFO dielectric phase [22,23]. However, it was observed that the position of the main peaks did not show any significant shift at various sintering temperatures, implying that the samples were formed well over the temperature interval. However, the samples sintered at the last three temperature points showed few or no BFO peaks, and only those sintered at 900 °C revealed a strong BFO peak near 27°, as highlighted with the pink ellipse in Fig. 1. This may have resulted from the mass of the Bi^{3+} ions begin to volatilize out of the samples. The synthesized temperature of Bi ferrites was near 900 °C [24].

As introduced in the experimental section, the original XRD patterns and phase composition were determined through Rietveld refinement. Finally, the observed and calculated patterns, and the discrepancy between them are shown in Fig. 2, which indicates that the calculated results are consistent with the observed results.

The results, such as cell parameters, site occupation and content of positive ions and reliabilities of refinement are listed in Table 1. From this table, it can be seen that all the Cd ions occupied A-sites, and Mg and Fe ions occupied both A-sites and B-sites. Meanwhile, as the temperature rose, the content of Mg ions at A-sites decreased while it increased at B-sites. Furthermore, the content of Fe ions changed in the opposite direction, indicating that some Mg ions migrated from A-sites to B-sites, and Fe ions migrated inversely as the temperature increased. In addition, the reliability of the refinement was verified by the comparatively low values of χ^2 , ωRp , and Rp listed in Table 1.

Fig. 3 displays the temperature-dependence of the samples with cross-section SEM images. From the figure, it can be concluded that all the spinel ferrites have a relatively homogenous grain distribution. Although there is little change in temperature in the experimental scope, the grains still show some growth tendencies, which can be described by the following two aspects. One is on density: as the temperature increases from 900 °C to 940 °C, the number of pores is reduced. At a temperature of 900 °C, many apparent voids coexist with grains over large areas, while as the temperature increases to 940 °C, very few pores can be observed, indicating that higher temperature brings about denser sintering samples. Another aspect is the average grain size, which increases monotonously with increasing temperature. Via a linear intercept method in statistics, the grain sizes were evaluated to be approximately 1.1 μm , 1.3 μm , 1.6 μm , and 2.1 μm , at the four corresponding temperature points. This reveals that higher temperature allows the grains to grow larger in size. To validate the above-mentioned explanation, the experimental densities (ED) measured by the Archimedes drainage method, the theoretical density (TD) calculated in the Rietveld refinement, and the relative densities calculated by ED divided by TD are listed in Table 2, which shows that the bulk density increases with increasing temperature.

The magnetic hysteresis loops and magnetic property (saturation

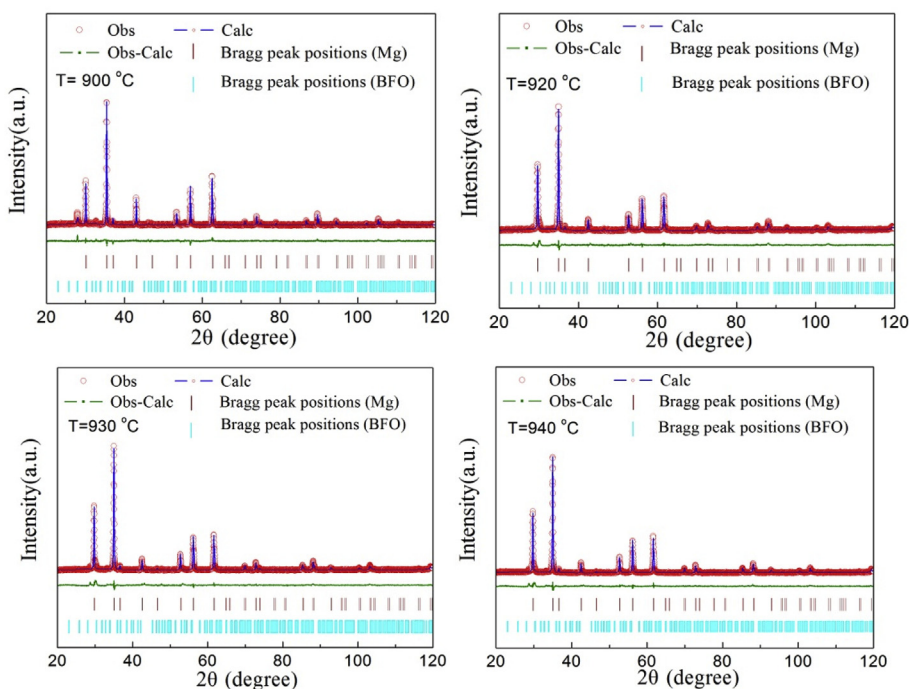


Fig. 2. Rietveld refinement results of the X-ray diffraction patterns of the samples sintered at various temperature points. The observed patterns (red rings), the best fit Rietveld profiles (dashed lines in blue), and difference between the observed pattern and the best-fit Rietveld profiles (solid line in olive), and Bragg peak positions of Mg ferrite (vertical segment in wine) and Bragg peak positions of BFO (vertical segment in cyan).

magnetization (M_s) and coercivity (H_c) curves of the samples sintered at different temperature points are shown in Fig. 4. The magnetic hysteresis loops in Fig. 4 (a) indicate the spinel ferrites have excellent soft magnetic properties. Moreover, the magnetization is enhanced with the increase in temperature, as shown in Fig. 4 (b). M_s changes with a significant monotonously increasing trend, and the concrete numerical values are 32.07 emu/g, 36.18 emu/g, 36.96 emu/g, and 37.94 emu/g with the corresponding temperatures of 900 °C, 920 °C, 930 °C, 940 °C. The change in the coercivity (H_c) with temperature exhibits a trend reverse to that of the saturation magnetization, meaning H_c monotonically decreases with the increase in temperature, with values of 105.6 Oe, 92.76 Oe, 63.75 Oe, and 60.5 Oe. The enhanced M_s and depleted H_c are evidence not only that the samples were well formed, but the magnetic properties change according to a regular trend with increasing temperature. Generally, what produces the larger value of M_s is the larger grain size as well as the higher density, caused by an increase in temperature. The theory of a dead layer, such as in the core-shell model, can be used to explain the similarly paced change in temperature and M_s [25,26]. In the model, the magnetic particles are assumed to be shielded inside a non-magnetic layer. The increase in the M_s can be attributed to the decrease in the presence of the dead layer. In addition, the variation in A-B site exchange interaction between tetrahedral (A) and octahedral (B) sublattices also explain the positively correlated relationship between grain size and M_s . Two different crystallographic sublattices exist for magnetic ions in spinel ferrites with cubic crystal texture: tetrahedral (A) and octahedral (B). The superexchange interaction between the ions in the A and B sublattices combined with oxygen ions has a primary influence on the magnetic order [27]. This is probably because Mg^{2+} ions occupies both the A-sites and B-sites, creating an irregular ion occupation distribution,

which is a key to determining the magnetic properties, especially the M_s and H_c . The cations in the magnetic materials occupy lattice sites to some extent depend on their special fondness for what they prefer in bulk materials, where the particle size determines the extent of inversion. In the experimental samples, as shown by the Rietveld refinement, Mg^{2+} and Fe^{3+} occupied both the A-sites and B-sites. As the temperature rose, Mg^{2+} ions migrated from A-sites to B-sites and Fe^{3+} migrated from B-sites to A-sites. This migration takes the edge off strains and a canted spin structure, which results from broken surface exchange bonds and weakens the A-B exchange interactions, causing an increase in the saturation magnetization with an increase in the grain size [28].

All the synthesized samples were measured via XPS, and there were no difference in the curves. The Fe2p spectra intensity depending on the binding energy of the samples sintered at 930 °C is displayed in Fig. 5. This figure indicates that the binding energy is 718.54 eV, 710.56 eV and 724.72 eV, correspondingly denoting the satellite peak, $Fe2p_{3/2}$, and $Fe2p_{1/2}$, which means that it is +3 valence, and not +2 valence for all the Fe ions [29]. The decreased coercivity (H_c), denoting the magnetic field intensity needed to diminish the magnetization to zero, is decreasing. There are two reasons for determining H_c , according to Gadkari et al. One is the relationship between the H_c and anisotropy constant of the magnetic materials according to the one-ion model, as the anisotropy constant depends on the content of Fe^{2+} ions [18]. Another reason is the microstructure: there are no Fe^{2+} ions in the sample, the above-mentioned increase in grain size is responsible for the decreased H_c . Simultaneously, a higher M_s also can lower the H_c , which can be explained by their relationship based on the Stoner-Wohlfarth theory [30]:

Table 1

Rietveld refinement results for the X-ray powder diffraction sample patterns with cell parameters, A-site ions, B-site ions, χ^2 , ωRp , R_p .

T (°C)	cell parameters (Å)	A-site	B-site	χ^2	ωRp	R_p
900	8.3920	(Mg _{0.23} Cd _{0.4} Fe _{0.37})	[Mg _{0.37} Co _{0.05} Fe _{1.58}]	1.26	1.57%	1.1%
920	8.5153	(Mg _{0.21} Cd _{0.4} Fe _{0.39})	[Mg _{0.39} Co _{0.05} Fe _{1.56}]	1.82	2.3%	1.5%
930	8.5146	(Mg _{0.2} Cd _{0.4} Fe _{0.4})	[Mg _{0.4} Co _{0.05} Fe _{1.55}]	1.97	2.38%	1.55%
940	8.5184	(Mg _{0.19} Cd _{0.4} Fe _{0.41})	[Mg _{0.41} Co _{0.05} Fe _{1.54}]	1.82	2.28%	1.55%

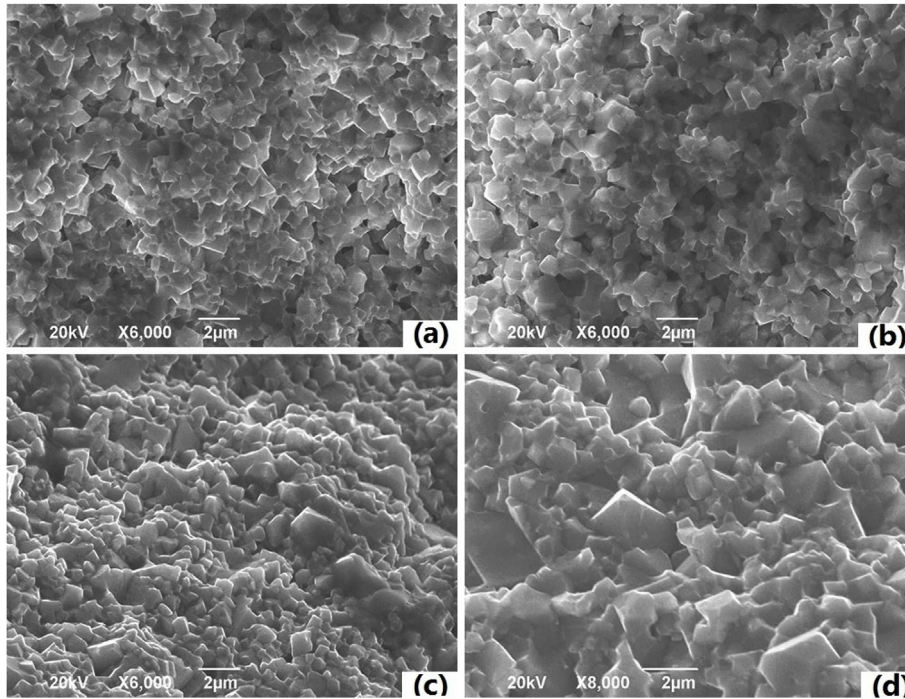


Fig. 3. SEM images of samples sintered at different temperature points. (a) 900 °C, (b) 920 °C, (c) 930 °C, (d) 940 °C.

Table 2
Relative densities of samples with various sintering temperature points.

T (°C)	900	920	930	940
relative densities	93.52%	95.08%	96.1%	96.52%

$$H_c = 0.98 K/M_s$$

Where K is the anisotropy constant. This relationship states that H_c is in inverse proportion to M_s , which is in good agreement with the change patterns of M_s and H_c , as discussed in the foregoing section.

Fig. 6 shows the magnetic spectrum and dielectric spectrum of the samples sintered at different temperature points. Fig. 6 (a) shows the change in the complex permeability measured over a long frequency range of 1 MHz-1 GHz. As the temperature increases, the real part of the permeability (μ') increases slowly from approximately 20 to 29. The increased temperature brings about larger grain size and denser sintering [31]. In ferrite materials, the initial permeability relies foremost on the saturation magnetization and the first-order anisotropy constant (K_{u1}), abiding by the following relationship [21]:

$$\mu \propto M_s^2 / K_{u1} + \lambda_s \delta$$

Where λ_s and δ represent the magnetization coefficient and internal

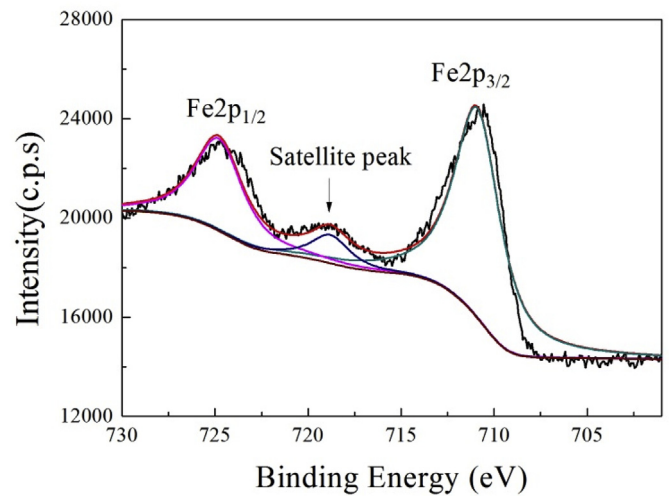


Fig. 5. Fe-2p XPS spectra of sample sintered at 930 °C.

stress, respectively. The term $\lambda_s \delta$ is small enough to be ignored for the small δ . Thus, the initial permeability is in positive correlation to the M_s . Thus, a higher M_s can also explain the increasing real permeability.

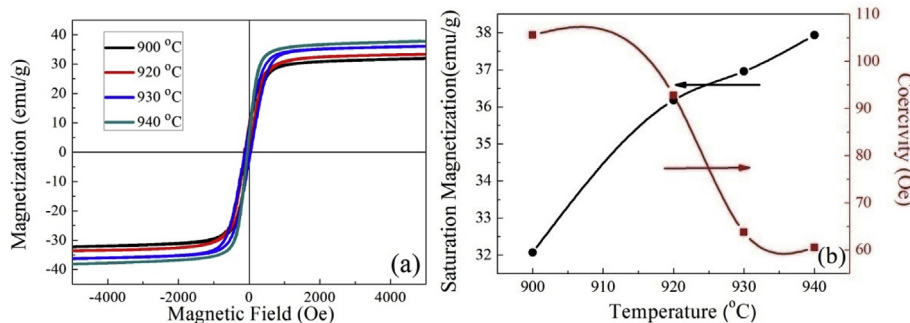


Fig. 4. Magnetic hysteresis loops (a) and magnetic properties (b) of samples sintered at different temperature points.

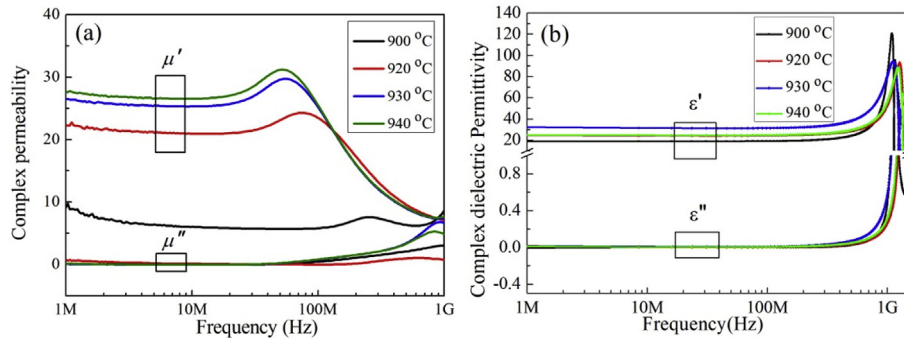


Fig. 6. (a) Complex magnetic permeability, (b) complex dielectric permittivity of samples sintered at different temperature points.

The imaginary part (μ'') of the samples remains at a fairly low level (approximately 0.7 for all samples) over the long frequency range. As a result, the magnetic tangent $\tan\delta_\mu$ is attained by equation [32]:

$$\tan\delta_\mu = \mu''/\mu'$$

Rendering an ultra low order of magnitude of $\tan\delta_\mu$ (approximately 3×10^{-2}) in the long frequency band.

However, the real part of the permittivity (ϵ') of the samples first increases from approximately 20 to 32 when the temperature increases from 900 °C to 930 °C, and then drops to 25 at 940 °C, as shown in Fig. 6 (b). In terms of the first three samples, with ϵ' increasing with the temperature, the enhanced dielectric properties may result from the larger crystal size and denser sample formation as shown in Fig. 3 [33]. For the temperature increase from 900 °C to 930 °C, the Bi_2O_3 sintering aid becomes liquid, then flows to the crystal boundary, helping and supporting the grain to grow and thus making the sintering denser with lower porosity. Meanwhile, the Bi_2O_3 aids combine Fe_2O_3 to form the dielectric material, BFO, which is a key to enhancing the real permittivity. However, as the temperature is more than 935 °C, some BFO grains begin to distort [34], causing a reduction in functional BFO in the dielectric materials. Thus, ϵ' is further reduced when the temperature goes up to 940 °C. As displayed in Fig. 6(b), the imaginary part of the permittivity (ϵ'') is quite low (approximately 0.09) in the frequency range for all samples. According to the computational formula of the dielectric loss tangent, $\tan\delta_\epsilon$ [35]:

$$\tan\delta_\epsilon = \epsilon''/\epsilon'$$

A surprisingly low magnitude of $\tan\delta_\epsilon$ of approximately 10^{-3} , and for some samples, as low as 10^{-4} is obtained.

Therefore, the equivalent permeability and permittivity characteristic of the samples sintered at 940 °C can be derived from Fig. 5. The figure shows that the samples sintered at 940 °C have almost equivalent μ' and ϵ' in the long frequency range of 1-100 MHz, providing an excellent application environment for ferrites used in antennas, as well as consummate impedance matching between antennas and the propagation medium.

In addition to that, the low-loss properties (low $\tan\delta_\epsilon$ and low $\tan\delta_\mu$) in Fig. 6 reveal that LTCC technology is an effective way to achieve this characteristic. Essentially, $\tan\delta_\mu$ is composed of three elements: the eddy current loss tangent $\tan\delta_e$, the hysteresis loss $\tan\delta_a$, the remaining loss tangent $\tan\delta_c$ [32,36]. Of these, $\tan\delta_e$ is caused by electromagnetic induction, causing energy loss in the material itself and hence generating power loss. Inside this material, the coercivity is the key to the electromagnetic induction. A uniform shape, fairly average grain size, uniform thickness of border grains, a small quantity of pores between the grains, and small anisotropy are the coexisting factors that lower $\tan\delta_a$. The proposed LTCC technology meets the requirements of these conditions. The last part, negligible $\tan\delta_c$, originates from Fe^{2+} ions, which were confirmed to be nonexistent in the samples.

The dielectric loss originates from a micromechanism [15,37]. In

particular, the grain boundaries between the single crystals and the polycrystalline ceramic are in dominant position to determine the dielectric loss. Apart from this, the pores inside the materials and grain size also give rise to $\tan\delta_\epsilon$ [38]. Generally, the formula below describes the relationship between porosity and $\tan\delta_\epsilon$ [15]:

$$\tan\delta_\epsilon = (1-P)\tan\delta_0 + CPn$$

In the formula, $\tan\delta_0$ represents the dielectric loss of materials with a dense structure, P is the porosity, and C is a material-dependent constant. As reported by Jia et al., the first term on the right-hand side denotes intrinsic loss, which is determined by the amount of processed materials, and the other term represents extrinsic loss, which depends on the imperfections [15]. As was discussed concerning the microstructure in the SEM images, the microstructure of the processed samples brings about comparatively low extrinsic dielectric loss, thus a low $\tan\delta_\epsilon$ is obtained.

As a whole, low magnetic and dielectric loss enables the proposed materials to possess excellent magnetic and insulating properties when used as an antenna substrate, due to the lower power loss caused by the heat.

4. Conclusions

In this work, magnetic and dielectric Mg–Cd ferrites with 2.5 wt% Bi_2O_3 were successfully processed at various temperature points via LTCC technology. The influence of microstructure on the magnetic performance and dielectric properties of the spinel Mg ferrites was studied in detail. Finally, the following conclusions could be drawn.

- 1). The spinel Mg–Cd ferrites obtained with densification-sintering LTCC technology had enhanced magnetic properties. For instance, the saturation magnetization (M_s) increased from 32.07 emu/g to 37.94 emu/g, while the coercivity (H_c) decreased from 105.6 Oe to 60.5 Oe, while the temperature rose from 900 °C to 940 °C.
- 2). The real part of the permeability (μ') increased monotonically from approximately 20 to 29, and the real part of the permittivity (ϵ') rose first from approximately 20 to 33, and then dropped to 25 with increasing temperature.
- 3). μ' and ϵ' were tailored to be equal ($\mu' \approx \epsilon' \approx 25$) over a long frequency range of 1-100 MHz at 940 °C. This may have resulted from the formation of the BFO dielectric materials and increased temperature.
- 4). Ultra low magnetic loss and dielectric loss were obtained ($\tan\delta_\mu \approx 0.035$, $\tan\delta_\epsilon \approx 0.003$). This is due to the densification sintering and low porosity.

The resulting desirable properties ensure that the proposed Mg ferrites would serve well for miniaturization, and would offer ease of integration for high frequency antennas.

Acknowledge

This work was supported by National Key Scientific Instrument and Equipment Development Project No.51827802, and by the National Nature Science Foundation of China (Nos. 51602036, 61371053 and 51672036), and Guizhou Province Key R&D Program (2016-3011).

References

- [1] L.B. Kong, Z.W. Li, G.Q. Lin, Y.B. Gan, Magneto-dielectric properties of Mg-Cu-Co ferrite ceramics: II. Electrical, dielectric, and magnetic properties, *J. Am. Ceram. Soc.* 90 (2007) 2104–2112.
- [2] H. Mosallaei, K. Sarabandi, Magneto-dielectrics in electromagnetics: concept and applications, *IEEE Trans. Antennas Propag.* 52 (2004) 1558–1567.
- [3] K. Buell, H. Mosallaei, K. Sarabandi, A substrate for small patch antennas providing tunable miniaturization factors, *IEEE Trans. Microw. Theory* 54 (2006) 135–146.
- [4] J.S. Colburn, Y. Rahmat-Samii, Patch antennas on externally perforated high dielectric constant substrates, *IEEE Trans. Antennas Propag.* 47 (1999) 1785–1794.
- [5] F.F. Manzillo, M. Ettore, M.S. Lahti, K.T. Kautio, D. Lelaidier, E. Seguenot, R. Sauleau, A multilayer LTCC solution for integrating 5G access point Antenna modules, *IEEE Trans. Microw. Theory* 64 (2016) 2272–2283.
- [6] J. Lee, J. Heo, J. Lee, Y. Han, Design of small antennas for mobile handsets using magneto-dielectric material, *IEEE Trans. Antennas Propag.* 60 (2012) 2080–2084.
- [7] L.A.A. Kishk, The effect of various parameters of circular microstrip antennas on their radiation efficiency and the mode excitation, *IEEE Trans. Antennas Propag.* AP-34 (1986) 969–976.
- [8] Esin Chang, Stuart A. Long, W.F. Richards, An experimental investigation of electrically thick, *IEEE Trans. Antennas Propag.* AP-34 (1986) 767–772.
- [9] R.C. Hansen, M. Burke, Antennas with magneto-dielectrics, *Microw. Opt. Technol. Lett.* 26 (2000) 75–78.
- [10] R.C. Hansen, Fundamental limitations in antennas, *Proc. IEEE* 69 (1981) 170–182.
- [11] A. Saini, K. Rana, A. Thakur, P. Thakur, J.L. Mattei, P. Queffelec, Low loss composite nano ferrite with matching permittivity and permeability in UHF band, *Mater. Res. Bull.* 76 (2016) 94–99.
- [12] A.K. Skrivervik, J.F. Zurcher, O. Staub, J.R. Mosig, PCS antenna design: the challenge of miniaturization, *IEEE Antennas Propag. Mag.* 43 (2001) 12–26.
- [13] M.T. Sebastian, H. Jantunen, Low loss dielectric materials for LTCC applications: a review, *Int. Mater. Rev.* 53 (2013) 57–90.
- [14] L.B. Kong, Z.W. Li, G.Q. Lin, Y.B. Gan, Electrical and magnetic properties of magnesium ferrite ceramics doped with Bi₂O₃, *Acta Mater.* 55 (2007) 6561–6572.
- [15] H.S. Jia, W.H. Liu, Z.Z. Zhang, F. Chen, Y.R. Li, J.L. Liu, Y. Nie, Monodomain MgCuZn ferrite with equivalent permeability and permittivity for broad frequency band applications, *Ceram. Int.* 43 (2017) 5974–5978.
- [16] T. Krishnaveni, S.R. Murthy, F. Gao, Q. Lu, S. Komarneni, Microwave hydrothermal synthesis of nanosize Ta₂O₅ added Mg-Cu-Zn ferrites, *J. Mater. Sci.* 41 (2006) 1471–1474.
- [17] R. Zahir, F.U.Z. Chowdhury, M.M. Uddin, M.A. Hakim, Structural, magnetic and electrical characterization of Cd-substituted Mg ferrites synthesized by double sintering technique, *J. Magn. Magn. Mater.* 410 (2016) 55–62.
- [18] A.B. Gadkari, T.J. Shinde, P.N. Vasambekar, Magnetic properties of rare earth ion (Sm³⁺) added nanocrystalline Mg–Cd ferrites, prepared by oxalate co-precipitation method, *J. Magn. Magn. Mater.* 322 (2010) 3823–3827.
- [19] A.B. Gadkari, T.J. Shinde, P.N. Vasambekar, Structural analysis of Y³⁺-doped Mg-Cd ferrites prepared by oxalate co-precipitation method, *Mater. Chem. Phys.* 114 (2009) 505–510.
- [20] A.B. Gadkari, T.J. Shinde, P.N. Vasambekar, Effect of Sm³⁺ ion addition on gas sensing properties of Mg_{1-x}Cd_xFe₂O₄ system, *Sensor. Actuator. B Chem.* 178 (2013) 34–39.
- [21] Y. Peng, X.H. Wu, Z.Y. Chen, W.H. Liu, F. Wang, X. Wang, Z.K. Feng, Y.J. Chen, V.G. Harris, BiFeO₃ tailored low loss M-type hexaferrite composites having equivalent permeability and permittivity for very high frequency applications, *J. Alloy. Comp.* 630 (2015) 48–53.
- [22] X.H. Zhu, E. Defay, Y. Lee, B. Andre, M. Aid, J.L. Zhu, D.Q. Xiao, J.G. Zhu, High permittivity Bi₂₄Fe₂O₃₉ thin films prepared by a low temperature process, *Appl. Phys. Lett.* 97 (2010).
- [23] P. Raksa, S. Pinitsoontorn, S. Maensiri, Structural, magnetic properties and dye-sensitized solar cells application of pure and La doped BiFeO₃ Powders prepared by sol-gel, *Ferroelectrics* 492 (2016) 150–158.
- [24] Q. Li, S.X. Bao, Y.L. Liu, Y.X. Li, Y.L. Jing, J. Li, Influence of lightly Sm-substitution on crystal structure, magnetic and dielectric properties of BiFeO₃ ceramics, *J. Alloy. Comp.* 682 (2016) 672–678.
- [25] R.S. Yadav, I. Kuřitka, J. Vilcakova, J. Havlicka, J. Masilko, L. Kalina, J. Tkacz, V. Enev, M. Hajdúchová, Structural, magnetic, dielectric, and electrical properties of NiFe₂O₄ spinel ferrite nanoparticles prepared by honey-mediated sol-gel combustion, *J. Phys. Chem. Solids* 107 (2017) 150–161.
- [26] Z. Karcioğlu Karakaş, R. Boncukcuoğlu, İ.H. Karakaş, M. Ertuğrul, The effects of heat treatment on the synthesis of nickel ferrite (NiFe₂O₄) nanoparticles using the microwave assisted combustion method, *J. Magn. Magn. Mater.* 374 (2015) 298–306.
- [27] M.H. Mahmoud, A.M. Elshahawy, S.A. Makhlof, H.H. Hamdeh, Synthesis of highly ordered 30nm NiFe₂O₄ particles by the microwave-combustion method, *J. Magn. Magn. Mater.* 369 (2014) 55–61.
- [28] M. Younas, M. Nadeem, M. Atif, R. Grossinger, Metal-semiconductor transition in NiFe₂O₄ nanoparticles due to reverse cationic distribution by impedance spectroscopy, *J. Appl. Phys.* 109 (2011) 093704.
- [29] M.Z. Naik, A.V. Salker, Tailoring the super-paramagnetic nature of MgFe₂O₄ nanoparticles by in³⁺ incorporation, *Mater. Sci. Eng., B* 211 (2016) 37–44.
- [30] S.E. Shirsath, S.S. Jadhav, B.G. Toksha, S.M. Patange, K.M. Jadhav, Influence of Ce⁴⁺ ions on the structural and magnetic properties of NiFe₂O₄, *J. Appl. Phys.* 110 (2011).
- [31] Z.L. Zheng, H.W. Zhang, J.Q. Xiao, Q.H. Yang, L.J. Jia, Low loss NiZn spinel ferrite-W-type hexaferrite composites from BaM addition for antenna applications, *J. Phys. D Appl. Phys.* 47 (2014).
- [32] G. Gan, H. Zhang, Q. Li, J. Li, X. Huang, F. Xie, F. Xu, Q. Zhang, M. Li, T. Liang, G. Wang, Low loss, enhanced magneto-dielectric properties of Bi₂O₃ doped Mg-Cd ferrites for high frequency antennas, *J. Alloy. Comp.* 735 (2018) 2634–2639.
- [33] A.S. Iyengar, D. Liang, X.P.A. Gao, A.R. Abramson, Densification effects on the electrical behavior of uniaxially compacted bismuth nanowires, *Acta Mater.* 60 (2012) 2369–2378.
- [34] G. Gan, H. Zhang, Q. Li, J. Li, M. Li, F. Xu, Y. Jing, Bi₂O₃ enhances magnetic and dielectric properties of low temperature co-fired Ba(CoTi)_{1.20}Fe_{9.6}O₁₉ ferrite composites in an oxygen atmosphere for applications in high frequency antennas, *Mater. Res. Bull.* 97 (2018) 37–41.
- [35] M.A. Dar, D. Varshney, Effect of d-block element Co²⁺ substitution on structural, Mossbauer and dielectric properties of spinel copper ferrites, *J. Magn. Magn. Mater.* 436 (2017) 101–112.
- [36] X. Batlle, X. Obradors, J. Rodríguez-Carvajal, M. Pernet, M.V. Cabañas, M. Vallet, Cation distribution and intrinsic magnetic properties of Co-Ti-doped M-type barium ferrite, *J. Appl. Phys.* 70 (1991) 1614–1623.
- [37] J.D. Breeze, J.M. Perkins, D.W. McComb, N.M. Alford, Do grain boundaries affect microwave dielectric loss in oxides? *J. Am. Ceram. Soc.* 92 (2009) 671–674.
- [38] S.J. Penn, N.M. Alford, A. Templeton, X.R. Wang, M.S. Xu, M. Reece, K. Schrapel, Effect of porosity and grain size on the microwave dielectric properties of sintered alumina, *J. Am. Ceram. Soc.* 80 (1997) 1885–1888.